

Received April 26, 2021, accepted May 22, 2021, date of publication June 14, 2021, date of current version June 30, 2021.

Digital Object Identifier 10.1109/ACCESS.2021.3089007

# Infrared Detection Method for Hypervelocity Impact Based on Thermal Image Fusion

XUTONG TAN<sup>1,2</sup>, XUEGANG HUANG<sup>2</sup>, CHUN YIN<sup>1</sup>, (Member, IEEE),  
SARA DADRAS<sup>3</sup>, (Senior Member, IEEE), YU-HUA CHENG<sup>1</sup>, (Senior Member, IEEE),  
AND ANHUA SHI<sup>2</sup>

<sup>1</sup>School of Automation Engineering, University of Electronic Science and Technology of China, Chengdu 611731, China

<sup>2</sup>Hypervelocity Aerodynamics Institute, China Aerodynamics Research and Development Center, Mianyang 621000, China

<sup>3</sup>Electrical and Computer Engineering Department, Utah State University, Logan, UT 84321, USA

Corresponding author: Xuegang Huang (emei-126@126.com)

This work was supported in part by the National Basic Research Program of China under Grant 61873305, Grant 61671109, and Grant U1830207; and in part by the Sichuan Science and Technology Plan Project under Grant 2018JY0410 and Grant 2019YJ0199.

**ABSTRACT** As the number of space debris has increased rapidly in recent years, it poses a major threat to the safety of spacecraft in space, and damage assessment for space debris hypervelocity impact is very important. In order to more comprehensively and accurately describe the damage defects in the infrared inspection data collected by infrared thermal imaging technology, this paper proposes an ultra-high-speed impact damage detection algorithm based on infrared reconstruction image fusion. The algorithm first preprocesses the obtained infrared thermal response image sequence and separates the damage features, and then applies a multi-objective evolutionary optimization algorithm to extract the typical transient thermal response, and then reconstructs the feature infrared images. Finally, image fusion based on guided filtering is performed on the damage reconstruction infrared images. In this paper, several reconstruction images that represent different types of impact damage defect are merged together to improve the detection ability of the algorithm. Infrared detection experiments on damaged specimens obtained from actual hypervelocity impacts verify the effectiveness of the proposed algorithm.

**INDEX TERMS** Infrared thermal image fusion, transient thermal response, hypervelocity impact, damage evaluation.

## I. INTRODUCTION

Space debris is generally defined as a space object that has lost its basic function and is distributed in an orbit around the Earth utilized by artificial Earth satellites, usually at an altitude of 100 – 40,000 km above the ground [1]. Since the first man-made satellite was launched in 1957, thousands of spacecraft of various types have been sent to earth orbit. With the increase of human space exploration activities, the amount of space debris has increased geometrically, including the mission rocket bodies and satellites themselves, rocket jets, discarded material from space missions, debris from collisions between space objects, etc., which have become the main source of pollution of the space environment [2], [3].

The associate editor coordinating the review of this manuscript and approving it for publication was Zhe Xiao<sup>1</sup>.

The space debris travels around the Earth's orbit at extremely high velocities, reaching 7–8 km/s, and some even exceeding 10 km/s [4]. Especially for the huge number of millimeter-level tiny space debris particles, the probability of hitting the spacecraft is higher due to the inability to track and avoid them. The form of damage caused by tiny space debris hitting spacecraft at hypervelocity is very complex, ranging from simple craters and cracks caused by initial impacts to intensive impact damage caused by chain impacts. For example, the secondary debris cloud formed by the impact of space debris on the buffer screen of the typical Whipple protective structure, as shown in Figure 1, its secondary impact on the rear wall will cause various types of damage, including visible surface damage such as perforations, tears, potholes, etc., and invisible subsurface damage such as faults, spalling, and bulges. Complex hypervelocity impact processes often bring complex damage effects, ultimately

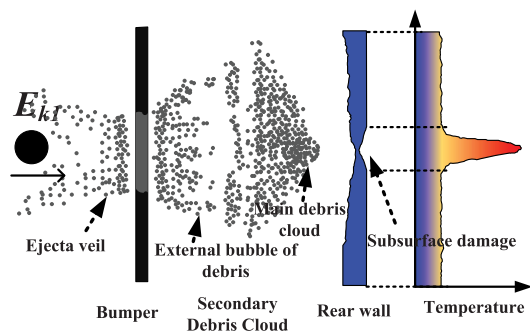


**FIGURE 1. Secondary debris cloud of hypervelocity impact for typical Whipple protective structure.**

forming complex multi-type defects coupling damage situation. For example, in the local area where the hypervelocity collision occurs, the behavior of the solid material is no longer a given solid material to ram and cause damage, but a similar compressible fluid acting in the center of the hypervelocity impact local area, resulting in completely different damage effect compared with that of a low-velocity, low-energy impact. Therefore, the type of damage caused by hypervelocity impact is complex, the amount of damage is huge, and the damage effect caused is completely different from that of low velocity and low energy impact. Therefore, how to detect and assess these complex hypervelocity impact damages comprehensively is an important research topic, which is very meaningful for space debris protection design, spacecraft maintenance support, and impact risk prediction.

The in-situ inspection and non-contact nature of infrared non-destructive testing is a great advantage considering the size and dimensions of the spacecraft and the fact that it is often difficult to disassemble. Secondly, infrared NDT is very fast and friendly to large area detection. Together with its high versatility, it is suitable for various materials and surface shapes of complex parts on spacecraft, such as metals and non-metals, making it a better detection method for spacecraft damage detection. Infrared inspection technology is a highly effective non-contact inspection method that is used in the aerospace field [5], [6]. The defect damage information is determined by monitoring the temperature field variation during the specimen heating process [7]. The processing of the acquired raw infrared thermal image sequences is a very important process in infrared NDT technology. Influenced by infrared thermal camera noise, heating inhomogeneity of excitation source, and different absorption rate of material surface, it leads to low reliability of defect information in a single frame of infrared image, and some subtle defect information may even be drowned out by noise. And a good infrared sequence thermal image processing technology can eliminate the interference of unfavorable factors, improve the signal-to-noise ratio, and enhance the defect displayability [8]–[11].

In order to efficiently derive damage information from IR thermal response sequences, many authors have

proposed corresponding image-based feature extraction algorithms, such as defect contrast enhancement methods, differential method, singular value decomposition, pulsed phase thermography, and ICA [12]–[14]. To some extent, they do achieve feature extraction. However, these methods have some drawbacks: the differential and singular value method decompositions lose temporal information about the image, and the frequency selection method for pulse phase requires human judgment. In addition, for compound coupling type defects and large size defects, it is difficult for the defect image detection algorithm through a single detection image to reflect a comprehensive, multi-detail, and holistic defect damage profile of the part under test. In recent years, a large number of scholars have also proposed distinctive detection algorithm frameworks in the field of infrared detection algorithms [15]–[17]. A large number of other effective feature extraction algorithms have been applied to the processing of infrared thermal image sequence data. Infrared thermal image sequence processing algorithms are continuously combined with other newer and more efficient algorithms [18]–[23]. However, their detection object, that is, the detection of the defect itself is relatively single. Usually a defect detection image with good detection effect for a single type of defect can be obtained. For hypervelocity impact and spacecraft complex types of defects are often missing to meet the detection needs of simultaneous detection of multiple types of defects. The problem of effective detection of complex multi-type defects at the same time needs to be solved, so our work effectively achieves the simultaneous detection of complex defects under hypervelocity impact based on the effective implementation of infrared data feature extraction combined with image fusion technology.

An excellent detection algorithm not only needs to be able to adaptively detect various types of defects from the infrared thermal response sequence accurately and efficiently, such as surface and subsurface defects that may be caused by hypervelocity impact. More importantly, it also needs to be able to extract fusion images that can represent multiple types and multiple defects at the same time. In order to facilitate subsequent tasks based on image segmentation, contour extraction, and quantitative analysis [24], the fused image also needs to be able to represent multiple details.

To solve the above problems, this article proposes an image fusion-based method for hypervelocity impact damage detection in infrared technology. The algorithm first extracts and acquires each defect type reconstruction image of the damaged specimen by the infrared damage information extraction algorithm and the infrared damage image reconstruction algorithm. The Density-Based Spatial Clustering of Applications with Noise clustering algorithm is used to achieve adaptive determination of the number of defect categories, which avoids the need to pre-determine the number of defect categories and separates the transient thermal response sets of defect categories from each other [25], [26]. Then, a multi-objective evolutionary optimization algorithm is used to extract the most representative transient thermal

response from the transient thermal response set of each category, and at the same time, the typical representative transient thermal response maintain the greatest difference from the transient thermal response sets of other categories [27], [28]. Finally, the extracted representative thermal responses are used to reconstruct the infrared defect images, which can fully characterize the defect features of a particular category.

Afterwards, multiple categories of defect information, multiple quantities of defect information, multiple details of defect information, etc. need to be fused together from each extracted IR reconstructed image. Commonly used image fusion algorithms include transform domain-based fusion algorithms based on pyramidal decomposition and wavelet transform-based fusion algorithms, but the fusion effect receives serious alignment effects [29]. In recent years, spatial domain-based fusion algorithms have attracted a lot of attention, such as pixel-based fusion and block-based fusion [30]. However, in damage assessment under hypervelocity impact, the quantity information, location information and contour information of the various defects formed due to the impact are very important. Wherein, the contour information is crucial for characterizing a defect, so the fusion algorithm needs to be able to efficiently preserve not only as much information as possible for each IR reconstruction, but also the edge contour information of the defects in each reconstruction. Then the image fusion algorithm based on guide filtering [31] is used to carry out infrared reconstruction image fusion. In the end, the above method realized the homologous heterogeneous coupling defect IR reconstruction image fusion, heterologous heterogeneous plural quantity IR reconstruction image fusion, and heterologous and homogeneous multi IR reconstruction image fusion. The research results ensure that the fused images are capable of accurately and clearly reflecting the comprehensive, multi-detail, and overall defect damage characteristics of the tested specimen. The main contributions of our work are shown below.

- 1) We propose a framework for the detection of complex multi-type coupled defect damage caused by hypervelocity impact on spacecraft. After data pre-processing, the damage detection framework first separates the transient thermal responses corresponding to different types of defects based on the transient thermal response(TTR) characteristics of each damage region using a clustering algorithm. The typical representative transient thermal response curves are then extracted from the different types of TTR sets, and image reconstruction is performed to achieve separate, clear, and highly detectable imaging of different types of defects. Finally, the detection images of different types of defects are fused by image fusion technology to achieve the simultaneous detection of complex multi-category defects.
- 2) In order to solve the problem of determining the number of complex classes of defects caused by

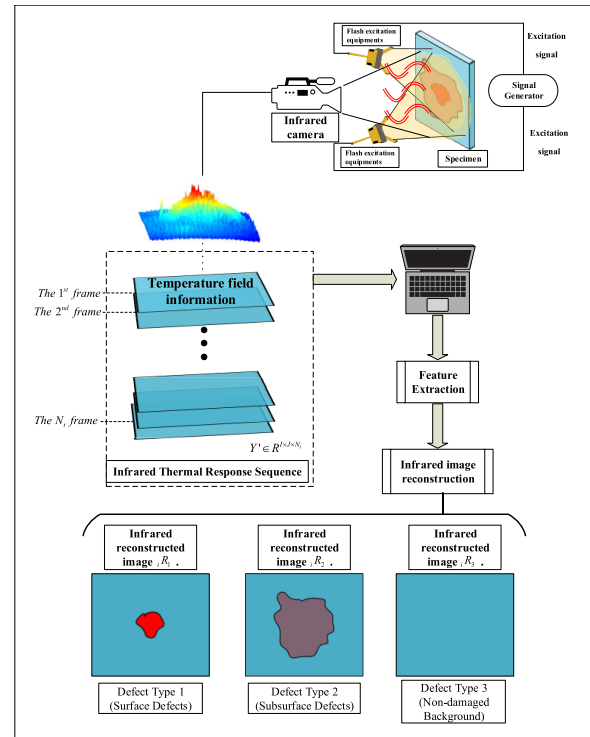


FIGURE 2. Infrared inspection platform.

hypervelocity impacts, we combined the density-based DBSCAN clustering algorithm to separate the transient thermal responses of different classes of defects from each other. It can avoid the problem that general clustering algorithms need to determine the number of defect classes manually in advance. Enables more accurate extraction of typical TTRs for each defect class, improving the detectability of reconstructed detection images for each individual defect class.

- 3) To achieve effective detection of complex types of defects simultaneously, a guided filter-based image fusion technique is used. Defect edge information can be retained in each individual type of defect detection image. The fused image can synthesize the defect feature information of each individual defect image. Solve the problem that a single detection image cannot simultaneously ensure clear imaging of complex categories of defects.

## II. PROBLEM STATEMENT

To obtain infrared reconstructed images that provide clear information about the characteristics of various types of defects, an infrared defect detection platform is adapted, as shown in Figure 2.

The excitation device generates different optical energy and thermal energy under the action of the excitation signal. Afterwards, the optical energy on the surface of the material is converted into thermal energy which can be detected and recorded by an infrared camera. Finally, an infrared

image sequence consisted of a series of recorded infrared images during the heating process is obtained. The thermal image sequence obtained is described as a matrix block ( $Y' \in R^{I \times J \times N_t}$ ), in which  $I, J$  represent the spatial information and  $N_t$  represents the time information. It contains a lot of damage information and non-damage information. Based on the infrared thermal response sequence, extract effective defect characteristics and perform infrared image reconstruction to obtain a reconstructed image that can clearly characterize the damage information.

Infrared thermal images are different from normal visible images. Infrared images are obtained by measuring the heat radiated from the object. A sequence of consecutive infrared thermal images constitutes the temperature change of the specimen during the entire heat transfer process. However, the raw infrared thermal image acquired solely by the thermal imaging camera has poor resolution, low contrast, low signal-to-noise ratio, and blurred visual effects. Directly based on the original infrared thermal image for defect detection is very poor. Therefore, infrared thermal image sequence data processing algorithm is very important. A well-designed thermal image processing technique for infrared sequences can eliminate the interference of unfavorable factors, improve the signal-to-noise ratio, and enhance the defect visibility. Therefore, our algorithm is of interest for the effective detection of defects, especially for the simultaneous detection of complex multiple types of defects in spacecraft caused by hypervelocity impacts.

In our previous works in [18], [19], a damage feature extraction for one IR thermal response sequence has been obtained, from which a series of IR reconstructed images of the specimen have been obtained. The  $k$ -th IR reconstructed image from the  $i$ -th IR thermal response sequence is denoted by  $iR_k$ . Each of the reconstructed images is reconstructed from a class of defects corresponding to a typical feature Transient Thermal Response (TTR), represents a specific type of damage, including different types of surface defects such as perforations, tears, pits, etc., as well as internal and subsurface defects such as spalling, delamination, and internal fractures. In order to facilitate subsequent image processing, including image stitching, image segmentation, and quantitative analysis, multiple surface and subsurface IR reconstructed images, such as  $iR_k$  and  $iR_l$ , of the same specimen that characterize different specific types of damage are fused together to enable the fusion images to characterize multiple damage information simultaneously and to obtain a more complete picture of the specimen's defects.

In addition, in the actual infrared inspection of defects, multiple measurements and local heating of the details are often required to obtain clearer information about the details and contours of the defects to obtain detailed infrared video stream data containing more details of the defect features. Based on the detailed IR thermal response sequence, a series of clearer defect detail reconstruction images can be reconstructed such as  $jR_m$ . In order to enhance the image detail,

it is also necessary to fuse the information contained in the IR reconstructed image that characterizes the detail portion of the image under multiple measurements, such as  $iR_k$  and  $jR_m$ , into the overall reconstructed image to enhance the overall image detection and defect detail contour information.

Therefore, image fusion is crucial in defect detection. The fusion of global image with global image can increase the image integrity, and the fusion of global image with local image can enrich the image details, both of which are beneficial for image detection. Therefore, this paper proposes the following image fusion-based algorithm for ultra-high-speed impact damage detection in infrared.

### III. IMAGE FUSION-BASED ALGORITHM FRAMEWORK FOR HYPERVELOCITY IMPACT DAMAGE DETECTION

#### A. ACQUISITION OF INFRARED RECONSTRUCTED IMAGES

During the data pre-processing, we performed a specific design for the thermal images. In order to utilize the different temperature response characteristics of each defect region throughout the heat transfer process, we extracted the feature information of each type of defect based on the transient thermal response. We used Pearson's correlation coefficient to measure the similarity of the thermal response features. Since the thermal response curves of the same type of defects in the heat conduction process are similar, we eliminate the redundant transient thermal responses with excessive similarity considering the detection rate and data size. In addition, since different types of defective regions, as well as non-defective regions, vary greatly in size, screening strategies with the same step size often lead to inefficient data searches, so we chunked the raw data. In different blocks of data, different block search steps are obtained based on the correlation situation within the block.

Since IR thermal response sequence data,  $M(r, c, t)$ , ( $r = 1, \dots, R_{max}; c = 1, \dots, C_{max}; t = 1, \dots, Frame_{max}$ ), contains a large amount of information, including spatial location of defective and non-defective pixels, temperature response, time variation information, etc., if the raw data is not pre-processed, the detection algorithm will be too long and the detection efficiency will be reduced, so it is necessary to pre-process the raw thermal response sequence data first.

Perform data pre-processing algorithm to remove repetitive redundant data. According to the position of the global maximum value  $M(R_m, C_m, T_m)$  in the infrared thermal response sequence, the Pearson correlation coefficient (PCC) of the thermal response sequence of it and other pixels in line with it,  $M(R_m, c, :)$ , ( $c = 1, 2, \dots, C_{max}, c \neq C_m$ ), is calculated to determine the appropriate column step size CSS. The original IR thermal response sequence is then divided into  $K + 1$  data blocks based on time thresholds  $THV_{ime}(k)$ . Find the location of the maximum value within each block and calculate the PCC between it and other pixel values within the block,  $PCC_{(k)M(k)R_{m,k}C_m, :}, k M(k)r, k C_m, :)$ , to determine the appropriate line step



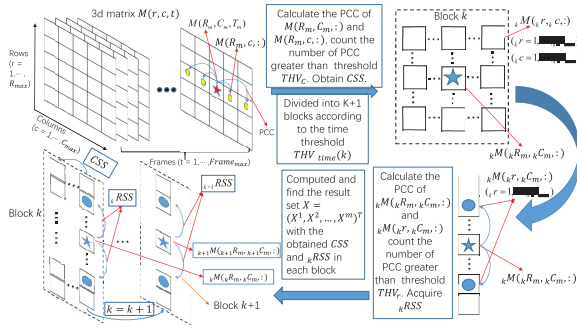


FIGURE 3. Data pre-processing process.

size  $kRSS$ . Finally, it searches for valid transient thermal response and removes repetitive transient thermal response based on the determined asynchronous step sizes in different blocks. The infrared data pre-processing algorithm is shown in Figure 3. The pseudocode of the data preprocessing is shown in Algorithm 1.

*Remark 1:* Each square represents a pixel point and each frame contains the temperature information of the specimen at the current moment. After the raw infrared data acquisition, a 3-dimensional temperature field information matrix  $M(r, c, t)$  is acquired. Based on the position of  $M(R_m, C_m, T_m)$ , search both sides and calculate the similarity of other pixels in the same row with it, counting the number of pixels with similarity greater than  $THV_C$  as the search column step  $CSS$ . Then the original 3-dimensional matrix  $M(r, c, t)$  is decomposed into  $k$  data blocks, and in each block the information is filtered using different search steps,  $kRSS$ . The search step size  $kRSS$  in each data block is mainly affected by the similarity between the local temperature maximum value  $kM(kR_m, kC_m, :)$  and other pixels in the same column within the block. The  $kRSS$  decision strategy is similar to that of  $CSS$ . Finally, the obtained different steps are used to sift redundant information within different blocks, and the pixel points with too much similarity are considered as redundant data and are discarded.

After that, the IR thermal data containing multiple structural characteristics of the specimens were obtained after variable step chunking feature data screening and repetitive data removal.

After obtaining the pre-processed transient thermal response set, it is necessary to separate the defective pixels from the non-defective ones and from the pixels with different classes of defects. In previous works [18], [19], Fuzzy C-means (FCM) and Bayesian classifiers are the effective clustering algorithms for transient thermal response set. However, they require user-defined number of clustering categories  $L$ . FCM and Bayesian classifiers cannot determine the number of clusters based on the characteristics of the data itself. In the actual inspection process, there is often no way to obtain the defect category information of the parts to be tested in advance, which requires the process of determining the number of defect categories after

**Algorithm 1** DATAPREPROCESSING

```

Input: Infrared Thermal Response Sequence,
 $M(r, c, t)$ , ( $r = 1, \dots, R_{max}; c = 1, \dots, C_{max}; t = 1, \dots, Frame_{max}$ ); Thresholds,  $THV_c$ ,  $THV_{time}(k)$ ,  $THV_r$  and  $THV_{pcc}$ ;
Output: TTR set,  $X = \{X^1, X^2, \dots, X^n\}$ ;
1:  $M(R_m, C_m, T_m) \leftarrow \max(M(r, c, t))$ ;
2:  $CSS \leftarrow \text{number of } PCC(M(R_m, C_m, :), M(R_m, c, :)) > THV_c, (c = 1, 2, \dots, C_{max}, c \neq C_m)$ ;
3: divide  $M(r, c, t)$  into  $k + 1$  blocks with  $THV_{time}(k)$ ;
4: for each block  $kM(kR_m, kC_m, :)$  do
5:  $kM(kR_m, kC_m, :) \leftarrow \max(kM(kR_m, kC_m, :))$ ;
6:  $kRSS \leftarrow \text{number of } PCC(kM(kR_m, kC_m, :), kM(kR_m, kC_m, :)) > THV_r, (kR = 1, 2, \dots, kR_{max}, kR \neq kR_m)$ ;
7: end for
8: Initialize TTR set,  $X, r = c = 1$ ;
9:  $n = 1, X^n \leftarrow kM(kR_m, kC_m, :)$ ;
10: while  $c < C_{max}$  do
11: Calculate  $PCC(kM(r, c, :), X^n)$ ;
12: if  $PCC(kM(r, c, :), X^n) < THV_{pcc}$  then
13:  $n = n + 1$ ;
14:  $X^n \leftarrow kM(r, c, :)$ ;
15: end if
16:  $r = r + kRSS$ 
17: if  $r > R_{max}$  then
18:  $k = k + 1, r = 1$ ;
19: end if
20: if  $r > R_{max}$  then
21:  $c = c + CSS$ ;
22:  $r = 1$ ;
23: end if
24: end while
25: return  $X$ ;

```

clustering, thus reducing the accuracy of the inspection algorithm. Therefore, this paper adopts the Density-Based Spatial Clustering of Applications with Noise Clustering algorithm (DBSCAN).

DBSCAN is a density-based clustering algorithm. It can find clusters of arbitrary shape in noisy spatial database without specifying the number of clusters in advance. The core idea of DBSCAN is to expand from a certain core point to the region where the density can be reached, so as to obtain a maximum region including core points and boundary points, and any two points in the region are connected by density. The DBSCAN algorithm pseudocode is shown in Algorithm 2. Obviously, the DBSCAN clustering algorithm can be used to achieve the adaptive separation between the transient thermal response of defective parts and the transient thermal response of non-defective parts, as well as the transient thermal response of different categories. Since the DBSCAN clustering algorithm is based on the characteristics of the data itself, there is no need to set the number of defect categories of the specimen in advance, and the automatic

**Algorithm 2** DBSCAN

**Input:** Pre-processed TTR data,  $X$ ; Clustering Parameters,  $eps$  and  $Minpts$ ;

**Output:** Clustering Result,  $Clu$ ;

- 1: Initialize core object set,  $\Omega = \emptyset$ , clustering number,  $l = 0$ , the set of unvisited TTRs,  $\Gamma = X$ , clustering result,  $Clu[l]$ ;
- 2: **for all** each  $X^n \in X$  **do**
- 3: Find eps-Neighbor of TTR  $X^n$ ,  $NE_{eps}(X^n) = \{X^m \in X \mid dist(X^n, X^m) \leq eps\}$ ;
- 4: **if**  $|NE_{eps}(X^n)| \geq Minpts$  **then**  
     , add TTR  $X^n$  to core object set,  $\Omega = \Omega \cup X^n$ .
- 5: **end if**
- 6: **end for**
- 7: **repeat**
- 8: In the set of core objects  $\Omega$ , randomly select a core object,  $X^i$ ;
- 9: Initializing the current cluster core object queue,  $\Omega_{current} = X^i$ , clustering number,  $l = l + 1$ . Initialize the current set of cluster samples,  $Clu[l] = X^i$ , Updating set of unvisited samples,  $\Gamma = \Gamma - X^i$ ;
- 10: **repeat**
- 11: Select a core object  $X^{i'}$  from the current cluster core object queue  $\Omega_{current} = X^i$ ;
- 12: Find all its eps-Neighbor,  $NE_{eps}(X^{i'})$ ;
- 13:  $\Delta = NE_{eps}(X^{i'}) \cap \Gamma$ ;
- 14:  $Clu[l] = Clu[l] \cup \Delta$ ,  $\Gamma = \Gamma - \Delta$ ;
- 15:  $\Omega_{current} = \Omega_{current} \cup (\Delta \cap \Omega) - X^{i'}$ ;
- 16: **until**  $\Omega_{current} == \emptyset$ , then  $\Omega = \Omega - Clu[l]$ ;
- 17: **until** The core object set,  $\Omega == \emptyset$ , Cluster end;
- 18: **return**  $Clu$ ;

discrimination of the number of defect categories can be realized.

*Remark 2:* In our work, in an attempt to solve the problem of simultaneous imaging of complex multiple types of defects, we first combine the DBSCAN algorithm to unsupervisedly cluster the thermal response curves of each type of defect, and then extract from them the typical transient thermal response of each type of defect for image reconstruction. The reconstructed images thus obtained are able to characterize each type of defect more clearly individually and specifically. In particular, the DBSCAN clustering algorithm is based on density clustering, which eliminates the need to set the number of defect categories in advance and solves the problem of unclear categories, numbers and locations of defects caused in hypervelocity impacts of spacecraft and the problem of difficulty in obtaining defect information manually in advance.

The  $dist(X^n, X^m)$  in Algorithm 2 is the Euclidean distance,  $dist(X^n, X^m) = \sqrt{\sum_{d=1}^D (X^n_d - X^m_d)^2}$ , wherein  $d$  is the dimensions of the TTR vector. After the DBSCAN clustering algorithm, the pre-processed TTR sets are clustered into  $L$

classes, which achieves the mutual separation of defect information and non-defect information, and the mutual separation of different classes of defect information.

It is then necessary to select a representative thermal response transient from each class set for quantitative analysis and subsequent image reconstruction operations. Ideally, the thermal response of a representative feature TTR should not only be sufficiently representative of the overall thermal properties of the set of transient thermal response categories in which it is located, but should also be sufficiently distinct from the thermal response of transients in other sets of categories. The above two metrics are often opposed to each other, so a decomposition-based MOEA/D multi-objective evolutionary optimization algorithm is used to extract the transient thermal response of each category of features, which was discussed in our previous work [3]. The multi-objective optimization problem is decomposed into a series of single-objective optimization sub-problems, and then an evolutionary algorithm is used to optimize these sub-problems simultaneously using the information from a certain number of neighboring problems, in order to avoid falling into a local optimum while maintaining the distribution of solutions.

In the detection process, the above two opposing objective functions are:

$$f_1(lX) = \min \sqrt{\sum_{d=1}^D ({}_lX_d - {}_lCen_d)^2} \quad (1)$$

$$f_2(lX) = \min \left\{ - \left( \sum_{l'=1, l' \neq l}^L \sqrt{\sum_{d=1}^D ({}_lX_d - {}_{l'}Cen_d)^2} \right) \right\} \quad (2)$$

where  $d$ , ( $d = 1, \dots, D$ ) represents the dimension of the TTR  $X$ .  $l$  and  $l'$ , ( $l, l' = 1, \dots, L, l \neq l'$ ) mean the  $l$ -th and  $l'$ -th class. The  ${}_lCen_d$  and  ${}_{l'}Cen_d$  represent the cluster center of  $l$ -th class and  $l'$ -th class.  $f_1(lX)$  represents the intra-class Euclidean distance inside the  $l$ -th class,  $f_2(lX)$  represents the total sum of inter-class distances between the  $l$ -th class and classes other than  $l$ . The multi-objective optimization problem is

$$\begin{aligned} \min F(lX) &= (f_1(lX), \dots, f_L(lX))^T \\ \text{sub to } lX &\in {}_l\Omega \end{aligned} \quad (3)$$

where  ${}_l\Omega$  is the range of the  $l$ -th class determined by the transient thermal response.  $L$  is the number of objective functions.  $f_i(lX)$  is the  $i$ -th objective function defined of  $l$ -th decision variable  $lX$ .

After selection of a representative feature transient thermal response based on a multi-objective evolutionary optimization algorithm, a thermal image need to reconstructed to represent the defect information by using the typical thermal response selected in the way of multi-objective evolutionary optimization. The following formula is used:  $R = \hat{C} * T$ , where  $R$  means reconstructed image,  $\hat{C}$  is the generalized inverse matrix of the matrix formed by the set of points

---

**Algorithm 3** Infrared Reconstruction Image Acquisition Algorithm
 

---

**Input:** Infrared Thermal Response Sequence,  $M$ ; Thresholds,  $THV_c$ ,  $THV_{time}$ ,  $THV_r$  and  $THV_{pcc}$ ; Clustering Parameters,  $eps$  and  $Minpts$ ; Iterative Termination Conditions,  $I$ ; Neighbor Size,  $n$ ; Population size,  $D$ ;

**Output:** Infrared Reconstruction Image,  $R$ ;

```

1:  $X = DATAPREPROCESSING$ ;
2:  $Clu = DBSCAN(X, eps, Minpts)$ ;
3: for each cluster  $Clu[l]$  do
4:   Decompose the multi-objective functions
       
$$\min g^{te}(X | \gamma, p^*) = \max\{\gamma_i | f_i(X) - p_i^*\}$$

5:   Initialization. Solution set,  ${}_lFV = []$ ; Define the neighbor of each weighted vector,  $N(k) = \{k_1, \dots, k_n\}$  ( $k = 1, \dots, D$ ), and its nearest  $n$  weight vectors are  $\gamma = (\gamma^{k_1}, \dots, \gamma^{k_n})^T$ , Randomly generated initialization population,  $X^1, \dots, X^D$ , initialize the reference point,  $p^*, p^* = (p_1^*, \dots, p_j^*, \dots, p_L^*)^T$ ,  $p_j^* = \min\{f_j(X) | X \in \Omega\}$ , ( $i = 1, \dots, L$ );
6:   while  $i < I$  do
7:     for each  $X^k$ , ( $k = 1, \dots, D$ ) do
8:       Randomly select two solutions from the neighbor  $N(k)$  of the  $k$ -th subproblem to generate a new solution  ${}_kX_{new}$  using evolution operator.
9:       for  $j = 1$  to  $L$  do
10:        if  $p_j^* < f_j({}_kX_{new})$  then
11:           $p_j^* = f_j({}_kX_{new})$ ;
12:        end if
13:      end for
14:      for  $j \in N(k)$  do
15:        if  $g^{te}({}_kX_{new} | \gamma, p^*) \leq g^{te}(X^j | \gamma, p^*)$  then
16:          replace  $X^j$  with  ${}_kX_{new}$ ;
17:        end if
18:      end for
19:      Keep the solution vector that dominates  $F({}_kX_{new})$  from  ${}_lFV$ , delete all solution vectors that are dominated by  $F({}_kX_{new})$ , if none of the vectors in  ${}_lFV$  dominate  $F({}_kX_{new})$ , add  $F({}_kX_{new})$  to  ${}_lFV$ ;
20:    end for
21:  end while
22: end for
23: Select a point from each  ${}_lFV$  as a representative transient thermal response to form a matrix,  ${}_lC = {}_lX_{RTTR}$ ;
24:  $T = reshape(M)$ ;
25:  $R = \hat{C} * T$ ;
26: return  $R$ ;
```

---

selected in the multi-objective evolutionary optimization, and  $T$  represents the  $2d$  matrix converted from the original  $3d$  matrix by column reconstruction. The overall process of extracting infrared reconstruction images from an infrared thermal response is shown in Algorithm 3.

As shown in Algorithm 3, the multi-objective evolutionary optimization algorithm first decomposes the original multi-objective problem using the Chebyshev method, then initializes it, calculates the Euclidean distance between the weight vectors, finds the nearest  $n$ -weight vector as the domain, and updates the population solution based on the aggregation function value. The Pareto Front is obtained, from which a Pareto optimal solution is selected as the transient thermal response of the representative features of each category. The IR image is reconstructed based on them.

After the above steps, the algorithm acquires a set of IR reconstructed images  $R$ . The  $k$ -th IR reconstructed image obtained from the  $i$ -th IR thermal response sequence is represented by  ${}_iR_k$ . Each reconstructed image is capable of clearly and individually characterizing the feature information of a particular type of defect. In order to obtain fusion images that characterize the integrity and richness of the defect features of defective specimens, it is necessary to fuse the different reconstructed images using image fusion techniques. In the field of infrared NDT, the original reconstructed image contains a large amount of information in which the defect information, including contour information, location information, size information, etc., is very important. In comparison, pixel-level image fusion preserves more of the original information. In the process of processing reconstructed images with defect information, the edge contour information of the defected part is one of the most important information to characterize a defect. Image fusion needs to meet the basic requirements as well as the edge retention function.

Therefore, how to make the edge contour information of the defect part clearer and more obvious is a crucial issue in reconstructed image processing. In recent years, many edge-preserving filters have been proposed, which are capable of smoothing the image while keeping the edges clear. Among them, the guide filter is a good edge-preserving filter. Its fusion only needs to acquire two scales of the image, which is efficient, and introduces the concepts of pixel saliency and spatial continuity of the image to improve the fusion effect while maintaining efficiency. It effectively retains the edge details of the image, so it is a good match for the flawed feature information retention and fusion requirements in reconstructed images. Figure 4 shows the process.

## B. IMAGE FUSION ALGORITHM BASED ON GUIDED FILTERING

The image fusion process based on guide filtering for IR reconstructed images is shown in Fig.(5). Fig.(5) shows a schematic diagram of the image fusion algorithm part of the detection algorithm framework. The schematic is divided into two parts A and B. Part A corresponds to III.A of the article, which is the stage of infrared reconstruction image acquisition for different defects, and the clear infrared reconstructed images obtained after part A characterizing different types of

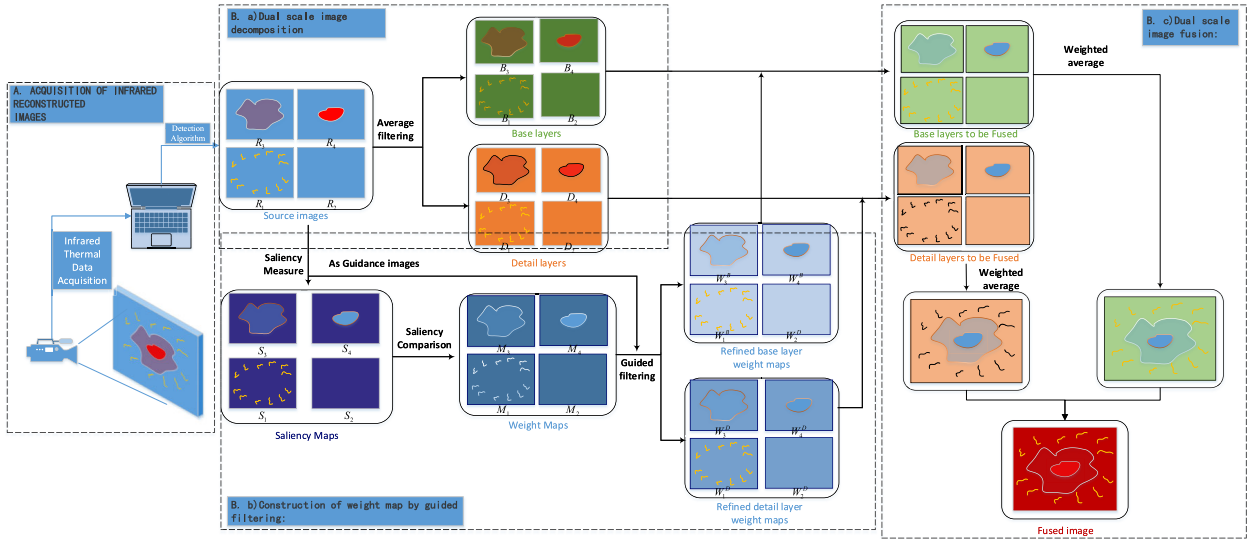


FIGURE 5. Image fusion process.

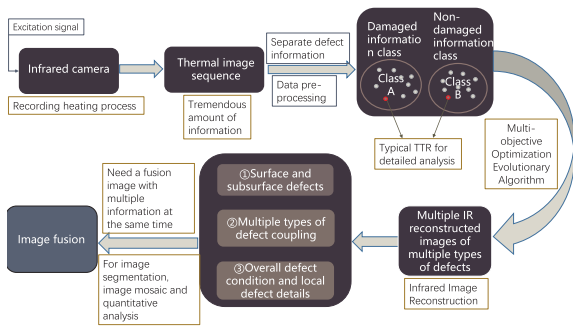


FIGURE 4. Defect detection process.

defects are noted as  $R_1, R_2, R_3, R_4$ . The individual infrared reconstructed images are used as input to part B to achieve image fusion to obtain a fused image that clearly characterizes all defective features. part B is divided into steps a, b and c. Step B.a) Firstly, the mean filtering is performed on each of the obtained infrared reconstructed images to obtain the base layer image characterizing the background information, namely  $B_1, B_2, B_3, B_4$ , and the detail layer image characterizing the existing defect information in each reconstructed image,  $D_1, D_2, D_3, D_4$ . Then, after step B.b), the original infrared reconstruction images without mean filtering are Laplacian filtered to obtain high-pass images and saliency detection is performed. The saliency maps of each image, which is represented by  $S_1, S_2, S_3, S_4$ , are obtained and the weight maps, namely  $M_1, M_2, M_3, M_4$ , of each infrared reconstruction image are obtained by comparing the saliency maps. Based on the obtained weight maps, the saliency maps are used as the guide images for the guide filtering to obtain the refined base layer weight maps,  $W_1^B, W_2^B, W_3^B, W_4^B$ , and detail layer weight maps,  $W_1^D, W_2^D, W_3^D, W_4^D$ . Finally, after step B.c), the decomposed individual base and detail layer

images are combined with the corresponding base and detail layer weight maps for weighted average fusion to obtain the final fused image.

### 1) IMAGE FUSION ALGORITHM BASED ON GUIDED FILTERING

The output  $O$  of the guided filter is a linear transformation of the guided image  $G$  in a local window centered at pixel  $k$ ,  $\omega_k$ .

$$O_i = \alpha_k^T G_i + b_k, \forall i \in \omega_k \quad (4)$$

wherein,  $\omega_k$  is a rectangular window of size  $(2r + 1) \times (2r + 1)$ ,  $\alpha_k$  is a coefficient vector of  $3 \times 1$ , and  $G_i$  is the color vector of pixel  $i$  in the guide graph.  $\alpha_k$  and  $b_k$  are constants in the rectangular window  $\omega_k$ . They can be obtained by minimizing the following variance formula between the input infrared reconstructed image  $R$  and the output image:

$$E(\alpha_k, b_k) = \sum_{i \in \omega_k} ((\alpha_k^T G_i + b_k - R_i)^2 + \varepsilon |\alpha_k|^2) \quad (5)$$

Herein,  $\varepsilon$  is a preset regularization parameter. Using a linear regression model,  $\alpha_k$  and  $b_k$  can be obtained as follows

$$\alpha_k = (\Sigma_k + \varepsilon U) \left( \frac{1}{|\omega|} \sum_{i \in \omega_k} G_i R_i - \mu_k \bar{R}_k \right) \quad (6)$$

$$b_k = \bar{R}_k - \alpha_k^T \mu_k \quad (7)$$

$\Sigma_k$  is a  $3 \times 3$  covariance matrix of the guide image  $G$  in the window  $\omega_k$ ,  $U$  is the identity matrix,  $\mu_k$  is the mean vector of the guide image  $G$  in the window  $\omega_k$  and  $|\omega|$  is the number of pixels in the window  $\omega_k$ ,  $\bar{R}_k$  is the mean of the input IR reconstructed image  $R$  in the window  $\omega_k$ . Because a pixel can be contained in multiple windows, the coefficients  $\alpha_k$  and  $b_k$



are averaged before filtering.

$$O_i = \bar{\alpha}_i^T G_i + \bar{b}_i \quad (8)$$

herein,  $\bar{\alpha}_i = \frac{1}{|\omega|} \sum_{k \in \omega_i} \alpha_k$ ,  $\bar{b}_i = \frac{1}{|\omega|} \sum_{k \in \omega_i} b_k$ . Henceforth, the guide filter operation is denoted by  $GF_{r,\varepsilon}(R, G)$ ,  $r, \varepsilon$  represent the filter parameters,  $R, G$  represent the infrared reconstructed images to be fused and the guided images, respectively.

## 2) GUIDED FILTER-BASED IMAGE FUSION PROCEDURE

The image fusion process based on guide filtering for IR reconstructed images is shown in Figure 5. First, a two-scale representation of the original infrared reconstructed images at the base and detail levels is obtained using mean value filtering, and then image fusion is performed using a weighted average fusion strategy based on guided filtering.

### a: DUAL SCALE IMAGE DECOMPOSITION

The source infrared reconstructed images to be fused are decomposed into base and detail layers by means of mean value filtering. The base layer image is derived from the following:

$$B_n = R_n * Z \quad (9)$$

herein,  $R_n$  is the  $n$ -th infrared reconstructed image to be fused, and  $Z$  is the mean filter, usually set to the scale size of  $31 \times 31$ . When the base layer image is acquired, the detail layer image is obtained by subtracting the base layer image from the source infrared reconstructed image.

$$D_n = R_n - B_n \quad (10)$$

Image decomposition decomposes the source image into a base layer with strong intensity variations at large scales and a detail layer with narrow intensity variations at smaller scales.

### b: CONSTRUCTION OF WEIGHT MAP BY GUIDED FILTERING

Each source infrared reconstructed image is filtered by Laplace filter to obtain high pass image  $H_n$ :

$$H_n = R_n * L \quad (11)$$

Herein,  $L$  is a Laplace filter of size  $3 \times 3$ . Then the saliency map  $S_n$  is constructed by using the local average of absolute value of high pass image  $H_n$ :

$$S_n = |H_n| * GF_{r_{gf}, \sigma_{gf}} \quad (12)$$

herein,  $GF$  is a Gaussian low-pass filter with size  $(2r_{gf} + 1) \times (2r_{gf} + 1)$  and parameter  $\sigma_{gf}$ . A saliency map is an impressive visual feature in an image that provides a good description of the level of saliency of image details. The saliency map is then used to determine the weighting map by the following equation:

$$P_n^k = \begin{cases} 1, & \text{if } S_n^k = \max(S_1^k, S_2^k, \dots, S_N^k) \\ 0 & \text{otherwise} \end{cases} \quad (13)$$

herein,  $N$  is the number of source infrared reconstructed images.  $S_n^k$  is the saliency value of the  $k$ -th pixel in the  $n$ -th source infrared reconstructed image. However, the resulting weight map is not aligned with the boundary of the actual reconstructed image, which affects the effect of the fused boundary. A well-suited strategy is to adopt the criterion of spatial consistency, based on which two adjacent pixels with similar brightness or color information shall carry similar weights. A common approach is to introduce an energy function that contains information about the saliency of the pixel, and the weights of the edge alignment are reinforced by a regularization term. The energy function is then minimized to obtain the desired weighting map.

Specifically, the fusion algorithm applies guide filtering to each weight map and adopts its corresponding input infrared reconstructed image as the guide image:

$$W_n^B = GF_{r_1, \varepsilon_1}(P_n, R_n) \quad (14)$$

$$W_n^D = GF_{r_2, \varepsilon_2}(P_n, R_n) \quad (15)$$

herein,  $W_n^B$  and  $W_n^D$  are the base level result map and the detail layer result map of the weight map after filtering,  $r_1, \varepsilon_1, r_2, \varepsilon_2$  are parameters for the corresponding guide filter, respectively. Finally, the  $N$  weight maps are normalized.

### c: DUAL SCALE IMAGE FUSION

Firstly, the image of the basic level and the detail layer is weighted average based on the weight map:

$$\bar{B} = \sum_{n=1}^N W_n^B B_n, \quad \bar{D} = \sum_{n=1}^N W_n^D D_n \quad (16)$$

Then, the final fused image is obtained by combining the weighted average of the base and detail layer images.

$$F = \bar{B} + \bar{D} \quad (17)$$

## C. DISCUSSION OF PARAMETER ISSUES

Our proposed algorithmic detection framework does involve a series of parameter settings. As presented in the above subsections, most of these parameters are configured with reference to empirical or general settings in general and with experimental validation and testing that can guarantee better detection results for our particular detection target. However, within certain reasonable limits, the defect detection performance of the algorithmic framework is insensitive to the impact of minor differences in the settings of the individual parameters in these subsections. The setting of the number of defect classes, which has the greatest impact on the detection effect, has been addressed by the density-based adaptive clustering algorithm during the algorithmic clustering process and no longer requires artificial settings. The results in most cases, the proposed algorithm can achieve good fusion and detection of complex multi-type defects. The experimental results can verify the good generality of the proposed algorithm to some extent.

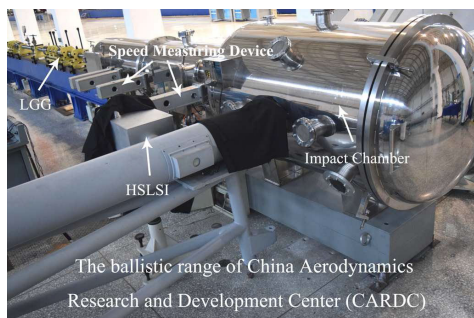


FIGURE 6. Setup for the hypervelocity impact experiment.

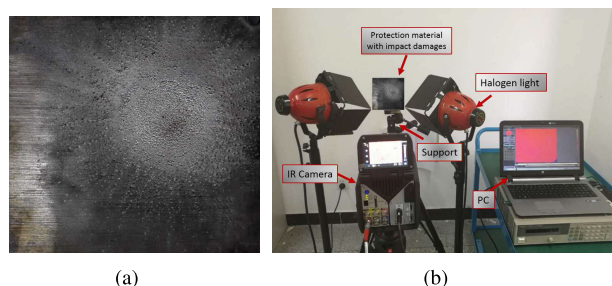


FIGURE 7. (a) The protection material with impact damages; (b) Experimental set-up.

#### IV. EXPERIMENTAL RESULTS

To verify the effectiveness and necessity of image fusion for defect detection in different types of specimens, several inspection experiments were performed, including those on defective specimens formed under real hypervelocity impact. The test results are as follows.

##### A. EXPERIMENTAL A

The defect conditions of defective specimen A were actually created under hypervelocity impact which was conducted in China Aerodynamics Research and Development Center (CARDC). The hypervelocity impact test as shown in Figure 6. The defective specimen A's defect includes surface impact crack and back spalling defects due to excessive impact force, which is shown in Figure 7(a). Therefore, a single infrared reconstruction of the defect features cannot represent both defects simultaneously, and the surface and sub-surface defect features can be effectively fused together using the image fusion algorithm in this paper.

##### 1) EXPERIMENTAL A: ACQUISITION OF INFRARED RECONSTRUCTED IMAGES

Due to the coupling of surface and subsurface defects in the same specimen caused by the hypervelocity impact, an inspection procedure was performed on specimen A shown in Figure 6(a). The results were as follows.

First, the experiment begins with an infrared thermal camera acquiring infrared thermal image sequences data, which is shown in Figure 7(b). The IR thermal image sequence

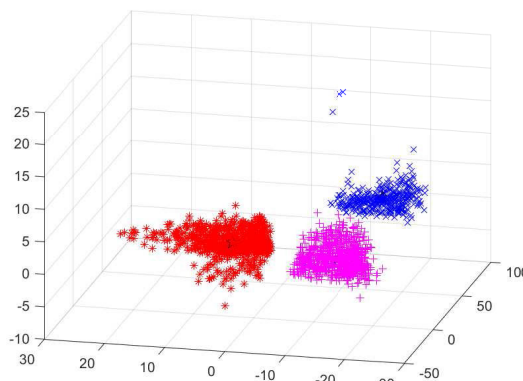


FIGURE 8. Result of clustering.

size is  $512 \times 640 \times 500$ , indicates that the infrared thermal response sequence contains a total of 500 frames of  $512 \times 640$  thermal image temperature field information data. The total number of pixels contained is 327680. After infrared data preprocessing, we got 2103 transient thermal responses.

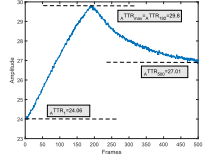
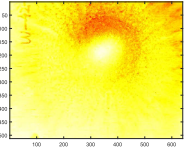
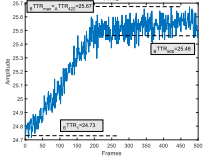
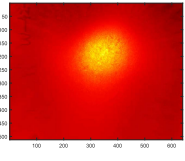
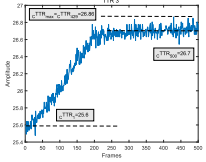
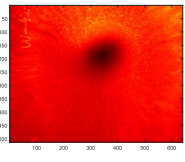
The 2103 transient thermal responses with redundant information removed were then clustered by DBSCAN clustering algorithm, herein, the 2103 transient thermal responses were divided into  $L = 3$  classes, each with 372, 927, 804 numbers, marked as Class A, Class B and Class C as shown in Figure 8. This represents the exist of 3 classes of structures with different thermal properties in our specimens, including the thermal response properties of the defect regions we need to characterize. Then a typical transient thermal response point for image reconstruction needs to be screened from each category. It should not only be guaranteed that the TTTR has a high similarity with other thermal response points of the same category, to prevent finding edge points and isolated points in the category, but also to ensure that the thermal response points with different categories also have a high degree of variability, so that the analysis of each category has a clear differences. Thus the multi-objective evolutionary optimization algorithm is executed in each category.

In the MOEA/D multi-objective optimization algorithm, set the weight vector number  $D = 40$ , i.e., the weight vector is  $\vec{\gamma}^1, \dots, \vec{\gamma}^{40}$ . The neighborhood range of each weight vector is set to number  $n = D \times 20\% = 8$ . And set the maximum number of iterations  $I_{max} = 200$ . The multi-objective function decomposition method chooses the penalty term based intersection method (PBI), and set the penalty term  $\alpha = 8$ . The multi-objective optimization target problem is set as follows:

$$\text{Class A : } \min F(1X) = (f_1(1X), f_2(1X), f_3(1X))^T$$

$$f_1(1X) = \sqrt{\sum_{d=1}^D (1X_d - 1Cen_d)^2}$$

**TABLE 1.** RTTR of each Classes and its transient thermal response curve of Specimen A.

Class	Transient Thermal Responses	Thermal image
Class A		
Class B		
Class C		

$$f_2(1X) = - \left( \sqrt{\sum_{d=1}^D (1X_d - 2Cen_d)^2} \right)$$

$$f_3(1X) = - \left( \sqrt{\sum_{d=1}^D (1X_d - 3Cen_d)^2} \right)$$

Class B :  $minF(2X) = (f_1(2X), f_2(2X), f_3(2X))^T$

$$f_1(2X) = \sqrt{\sum_{d=1}^D (2X_d - 2Cen_d)^2}$$

$$f_2(2X) = - \left( \sqrt{\sum_{d=1}^D (2X_d - 1Cen_d)^2} \right)$$

$$f_3(2X) = - \left( \sqrt{\sum_{d=1}^D (2X_d - 3Cen_d)^2} \right)$$

Class C :  $minF(3X) = (f_1(3X), f_2(3X), f_3(3X))^T$

$$f_1(3X) = \sqrt{\sum_{d=1}^D (3X_d - 3Cen_d)^2}$$

$$f_2(3X) = - \left( \sqrt{\sum_{d=1}^D (3X_d - 1Cen_d)^2} \right)$$

$$f_3(3X) = - \left( \sqrt{\sum_{d=1}^D (3X_d - 2Cen_d)^2} \right)$$

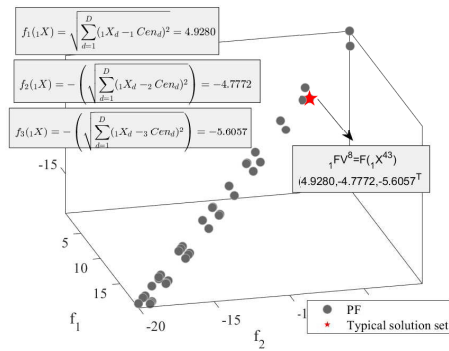
After the evolutionary algorithm, the representative transient thermal responses and their corresponding infrared reconstruction images are shown in Table 1. The Pareto Fronts of each class are shown in Figure 9. Representative transient thermal response points that can maintain

a high correlation with similar transient thermal response points while maintaining a high variability with non-identical transient thermal response points have been extracted by multi-objective evolutionary optimization algorithms. The point selected by Multi-objective evolutionary optimization algorithm of Class A in Function Value is  $1FV^8 = F(1X^{43}) = (4.9280, -4.7772, -5.6057)^T$ . Its corresponding transient thermal response vector after dimensionality reduction is  $1X^{43} = (3.5327, -3.5405, -3.6038)$ . In Class B, the selected point's Function Value is  $2FV^7 = F(2X^{72}) = (5.9319, -6.0718, -6.7283)^T$ . Its corresponding transient thermal response vector after dimensionality reduction is  $2X^{72} = (4.1167, -4.5881, 1.1014)$ . In Class C, the selected point's Function Value is  $3FV^{20} = F(3X^{56}) = (4.3031, -4.8562, -4.9423)^T$ . Its corresponding transient thermal response vector after dimensionality reduction is  $3X^{56} = (0.2225, 4.8870, -2.2895)$ .

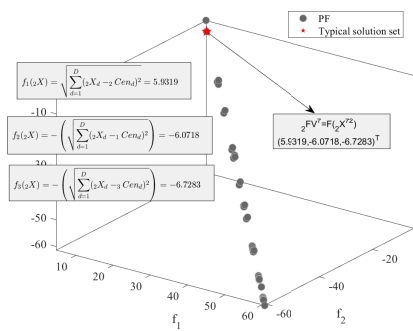
2) EXPERIMENTAL A:IMAGE FUSION ALGORITHM BASED ON GUIDED FILTERING

After obtain the 3 infrared reconstructed images,  $1R_A$ ,  $1R_B$  and  $1R_C$ , we can see that image  $1R_A$  corresponds to the structure type as the background region,  $1R_B$  to the structure region as the subsurface spalling defect, and  $1R_C$  to the structure region as the surface impact crack, and their corresponding damage regions have been highlighted in the reconstructed image. However, a single infrared reconstruction map can only highlight one type of defect, and for better detection and subsequent processing, different types of defect features need to be fused into a single map. The surface defects and subsurface defects of specimen A are highlighted in Figure 10 separately, we can see that a single reconstructed IR image is missing certain defect information, so useful complementary information from different reconstructed images needs to be extracted and fused into one image.

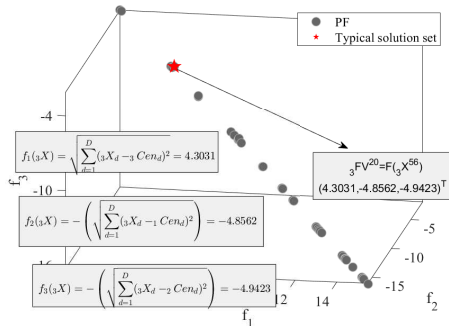
Then perform infrared reconstructed image fusion of  $1R_B$  and  $1R_C$  based on guide filtering. The result of fusion is shown in Figure 11. The fused infrared reconstructed image obtained by the guided filtering based fusion method can well preserve the complementary information of different source infrared reconstructed image such as the central cratering defects due to hypervelocity impact and the surrounding crack defect caused by secondary debris clouds. From this figure, it can be seen that the proposed detection algorithm can well preserve the brightness and color of the different defects, providing an enhanced quality of defect feature fusion image for more accurate and efficient defect detection and quantification. Besides, the fused image is not blurred, and the detection algorithm does a good job of protecting the focus areas of different source infrared reconstructed images without creating any artifacts that are non-existent, which means our algorithm has high robustness. As can be seen, our algorithm does implement defects color, good retention profile and details, can well preserve the complementary information of source infrared reconstructed images without producing artifacts and distortions.



(a) Pareto Front of Class A



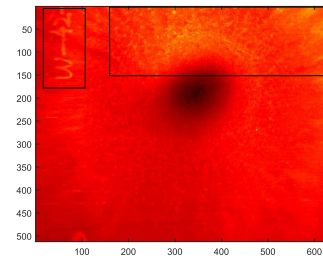
(b) Pareto Front of Class B



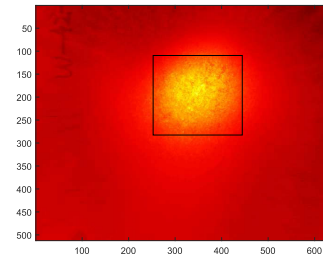
(c) Pareto Front of Class C

FIGURE 9. Pareto Front of Specimen A.

Firstly, the source infrared reconstruction image  ${}_1R_B$  and  ${}_1R_C$  are decomposed in two scales to obtain the base and detail images respectively, then Laplace filtering is performed to obtain the high-pass image, and then a saliency map is established based on the high-pass image, and the parameters are  $\sigma_{gf} = r_{gf} = 5$  to obtain the preliminary weight map, afterwards, the guide filter parameters are set to  $r_1 = 8, \varepsilon_1 = 0.0900, r_2 = 4, \varepsilon_2 = 0.0025$  to filter the weight map to obtain  $W_1^B, W_1^D, W_2^B,$  and  $W_2^D$  respectively. The process of fusion is shown in Figure 12. As shown in Figure 12, thanks to our algorithm that makes full use of the strong correlation between adjacent pixels to correct the noise and the deviation of the weight estimation that may be caused by the measurement of the saliency map as shown in the figure, thus achieving a better fusion Effect, and also improved robustness.



(a) surface defects of Class A



(b) surface defects of Class A

FIGURE 10. Defects in Specimen A.

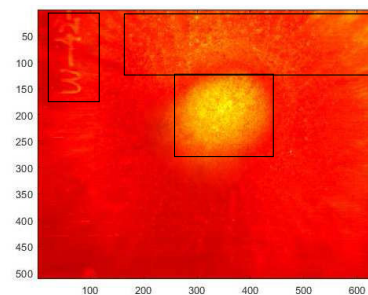


FIGURE 11. Result of infrared thermal image fusion.

B. EXPERIMENTAL B

The defect condition of specimen B is a man-made defect specimen. The specimen contains 3 rows of internal inclusion defects which are invisible, as shown in Figure 13. Each row consists of a series of circular holes of different sizes. The circular holes are filled with materials with different thermal conductivity to simulate super subsurface defects that may be formed under hypervelocity impact. Since that there are too many defects, three rows of defects called upper, middle and lower layers in specimen B. Each row of defects consists of 5 circular holes of different sizes, in order to obtain more accurate and more detailed defect information. Because that it is difficult to obtain sufficient inspection accuracy in a single inspection, we conducted three inspections on specimen B, and carried out detailed inspections for the upper, middle and lower defects respectively. And then our proposed algorithm will be used to perform image fusion on the three-line defect feature infrared reconstructed image.



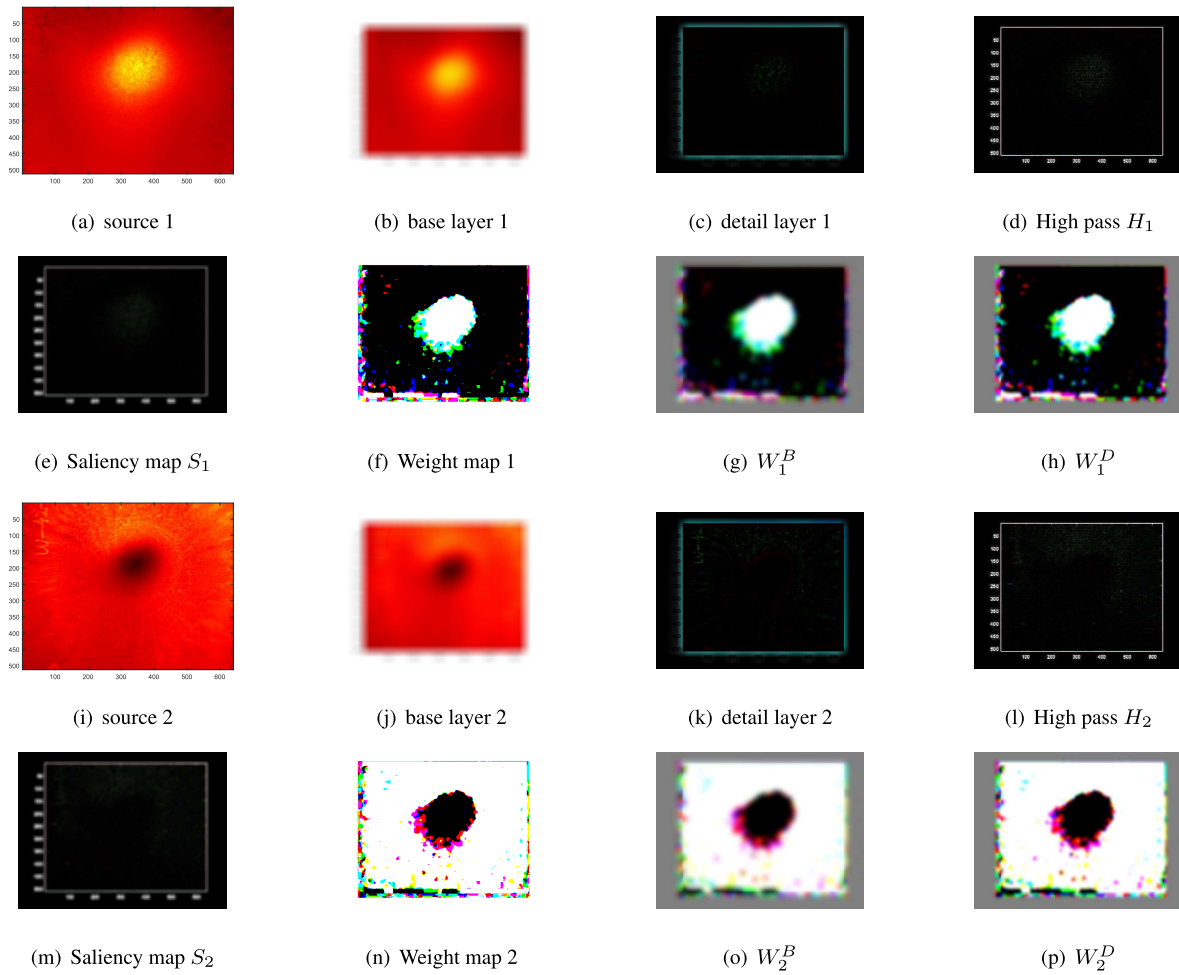


FIGURE 12. Fusion process of specimen A.

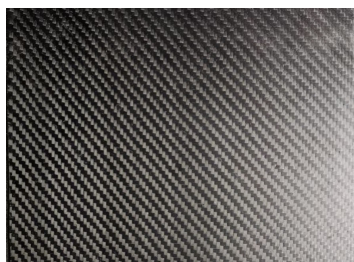


FIGURE 13. The surface of the specimen with internal inclusion defects.

1) EXPERIMENTAL B:ACQUISITION OF INFRARED RECONSTRUCTED IMAGES

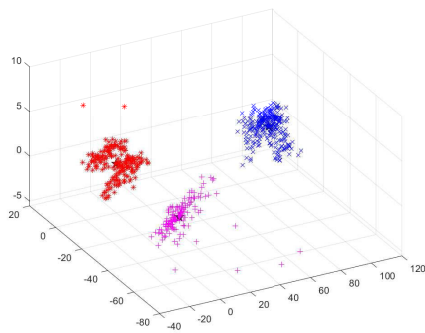
Due to the excessive number of defects, we carried out targeted inspections on the upper, middle and lower layers of specimen B. The results were as follows.

First, the IR thermal image sequence size is  $512 \times 640 \times 150$ , indicates that the infrared thermal response sequence contains a total of 150 frames of  $512 \times 640$  thermal image temperature field information data. The total number of pixels contained is 327680. After infrared data preprocessing, for

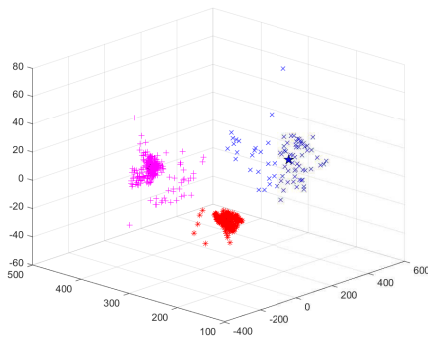
the upper layer, we got 1047 transient thermal responses. For the middle layer, 873 transient thermal responses were obtained. For lower layer, the number of obtained transient thermal responses is 1226.

The transient thermal responses were also divided into  $L = 3$  classes by DBSCAN, each with 251, 337, 459 numbers for upper layer, 198, 273, 402 for middle layer, 453, 396, 377 for lower layer. marked as Class A, Class B and Class C as shown in Figure 14. Then a typical transient thermal response point for image reconstruction needs to be screened from each category. It should not only be guaranteed that the TTTR has a high similarity with other thermal response points of the same category, to prevent finding edge points and isolated points in the category, but also to ensure that the thermal response points with different categories also have a high degree of variability, so that the analysis of each category has a clear differences. Thus the multi-objective evolutionary optimization algorithm is executed in each category.

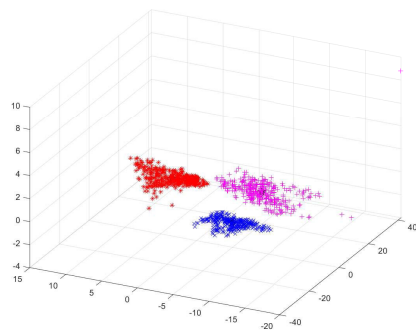
In the MOEA/D multi-objective optimization algorithm, also set the weight vector number  $D = 40$ , i.e., the



(a) upper layer



(b) middle layer

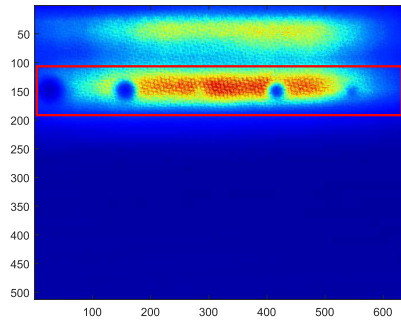


(c) lower layer

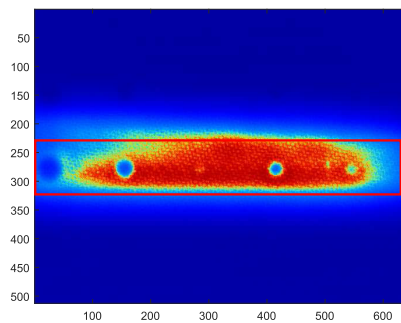
**FIGURE 14. Clustering result for Specimen B.**

weight vector is  $\vec{\gamma}^1, \dots, \vec{\gamma}^{40}$ . The neighborhood range of each weight vector is set to number  $n = D \times 20\% = 8$ . And set the maximum number of iterations  $I_{max} = 100$ . The multi-objective function decomposition method chooses the penalty term based intersection method (PBI), and set the penalty term  $\alpha = 5$ . The multi-objective optimization target problem is set the same as specimen A.

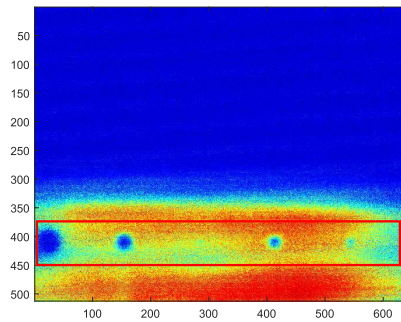
After the evolutionary algorithm, the Pareto Front, infrared reconstruction images, and transient thermal response curves for each category of upper layer, middle layer, and lower layer are shown in Table 2, Table 3, and Table 4, respectively. From the IR reconstruction images of three detections,



(a) upper layer defects of Specimen B



(b) middle layer defects of Specimen B



(c) lower layer defects of Specimen B

**FIGURE 15. Defects in Specimen B.**

it can be seen that due to the excessive number of defects in the specimen at the same time, it is difficult to extract all defects at the same time in one detection, so it is necessary to perform multiple detections on different regions. Then, we need to pick out the detail feature image of the defect part that we are interested in, from the IR reconstructed images obtained in each inspection, and fuse the defect detail feature images from the 3 inspections so that we get the detail feature case of the 3 layers simultaneously in one image.

## 2) EXPERIMENTAL B: IMAGE FUSION ALGORITHM BASED ON GUIDED FILTERING

After three times of testing, a series of infrared reconstruction images about specimen B are obtained, including the

TABLE 2. Pareto Front, Transient thermal response and Infrared reconstructed images of upper layer.

Detection 1	Upper layer		
Class	Class A	Class B	Class C
Pareto Front			
TTR curve			
IR reconstructed image			

infrared reconstruction images which represent each line of defect details,  $1R_B$ ,  $2R_B$  and  $3R_B$ . Through the infrared reconstruction image, we can see that  $1R_B$  can clearly show the location and shape of the defects in the upper layer,  $2R_B$  can represent the size and location of several defects in the middle layer, and  $3R_B$  can clearly show the specific characteristics of the bottom layer defects, their corresponding defect area feature information has been highlighted in the infrared reconstruction images. Because it is difficult to characterize so many defects, so various of sizes, and so many types of defects simultaneously in a single infrared reconstruction image, it is necessary to fuse the details of individual defects from multiple measurements into a single fused image. The defects of specimen B are highlighted in Figure 15. As shown in Figure 15, the picked three IR reconstruction images,  $1R_B$ ,  $2R_B$  and  $3R_B$ , do have the details of the three-layer defects that we are interested in.

Then perform infrared reconstructed image fusion of  $1R_B$ ,  $2R_B$  and  $3R_B$  based on guide filtering. The result of fusion process is shown in Figure 16. It can be seen that our algorithm can still effectively preserve the edge and detail features of defects in each detection for the infrared reconstructed image which is not obtained by the same detection, and realize the fusion of multiple information.

Finally, the source infrared reconstruction image  $1R_B$ ,  $2R_B$  and  $3R_B$  are decomposed in two scales to obtain the base and detail images respectively, then Laplace filtering is performed to obtain the high-pass image, and then a saliency map is established based on the high-pass image, and the parameters are set the same  $\sigma_{gf} = r_{gf} = 5$  to obtain the preliminary weight map, afterwards, the guide filter parameters are set to  $r_1 = 8$ ,  $\varepsilon_1 = 0.1100$ ,  $r_2 = 4$ ,  $\varepsilon_2 = 0.0030$  to filter

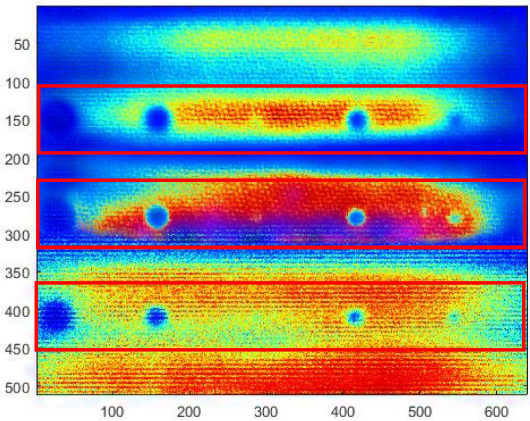


FIGURE 16. Result of infrared thermal image fusion.

the weight map to obtain  $W_1^B$ ,  $W_1^D$ ,  $W_2^B$ ,  $W_2^D$  and  $W_3^B$ ,  $W_3^D$  respectively. The final result of fusion is shown in Figure 17. As can be seen from the final fused image, our algorithm is able to achieve good fusion results for IR defect details that are not reconstructed from the same inspection, and the fused image is able to retain valuable defect edge detail information from each inspection without creating blurred and artificial areas.

*Remark 3:* To illustrate the effectiveness of our detection framework, the detection results of TSR, ICA, and PCA algorithms based on the same raw infrared thermal image sequence data from our experiments A and B have been used for comparison with our algorithm. Since our algorithm clusters the transient thermal responses of different types of defects, it is able to extract the typical thermal response curve of each type of defects during heat conduction

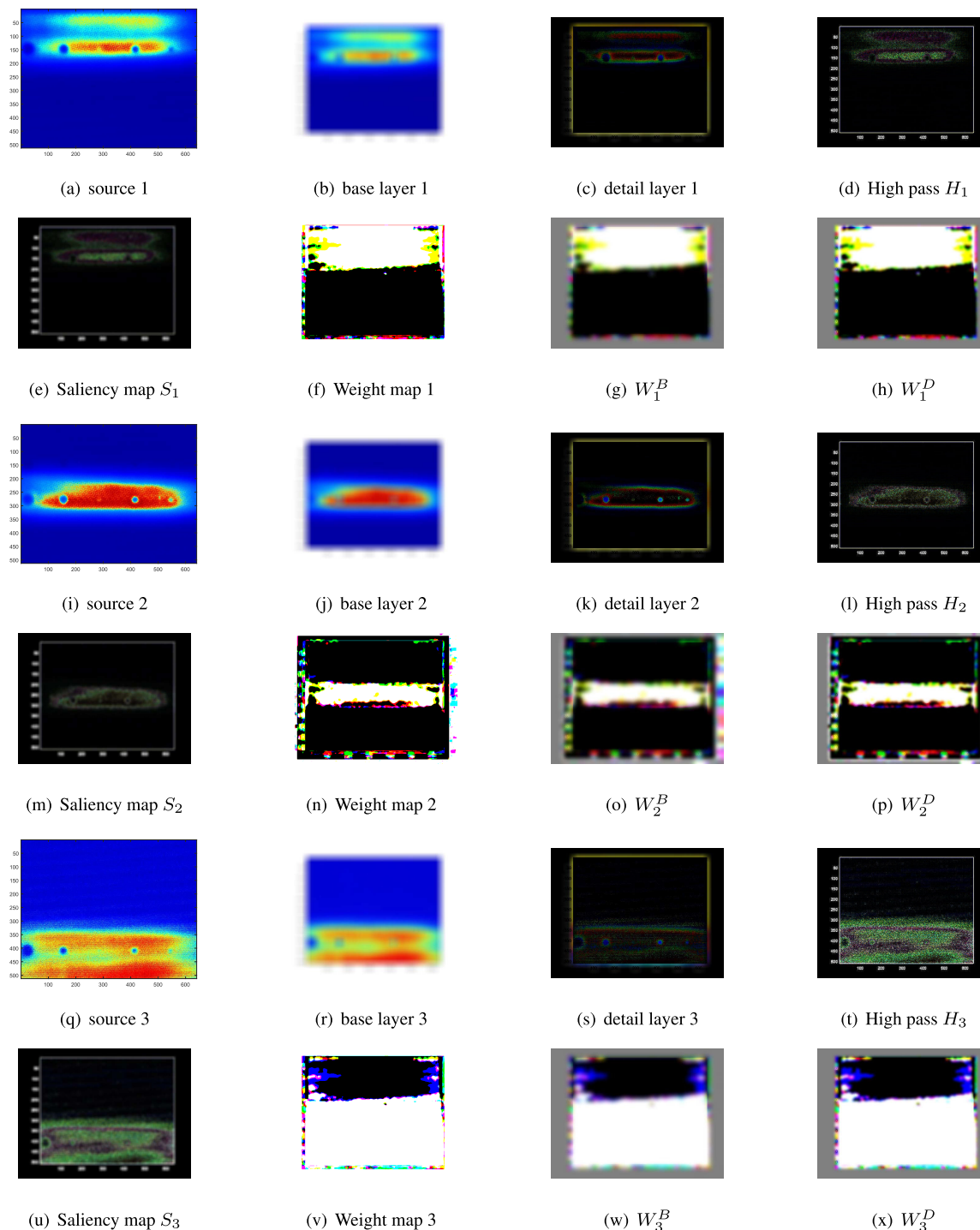


FIGURE 17. Fusion process of Specimen B.

and perform defect reconstruction based on them. The comparison results show that the reconstructed thermal images (Our subsection III-A.) of each type of defect based on the typical transient thermal response have higher detectability, distinct defect characteristics, higher contrast, and less noise

information than the detection images of TSR, ICA, and PCA algorithms. After individual imaging of each type of defect, our image fusion section (subsection III-B) enables simultaneous detection and clear imaging of complex types of defects.



TABLE 3. Pareto Front, Transient thermal response and Infrared reconstructed images of middle layer.

Detection 2	Middle layer		
Class	Class A	Class B	Class C
Pareto Front			
TTR curve			
IR reconstructed image			

TABLE 4. Pareto Front, Transient thermal response and Infrared reconstructed images of lower layer.

Detection 3	Lower layer		
Class	Class A	Class B	Class C
Pareto Front			
TTR curve			
IR reconstructed image			

V. CONCLUSION

Due to the different thermal performance characteristics reflected by the transient thermal response of each feature, different reconstructed images have completely different descriptions of the defective specimens. The fusion algorithm takes advantage of the complementary nature of two or more defect reconstructed images in terms of defect type and defect feature information, so that the fused images have a more comprehensive and clearer description of the specimen's defect characteristics. It can enhance the fuzzy feature information in the single source image and restore the

missing information in the image to improve the ability of image stitching, detection, classification and identification. Nevertheless, there are areas of our work that need to be improved in the future work.

- 1) The effect of clustering algorithm depends on the selection of clustering parameters, more advanced and adaptive clustering algorithms should be adopted in the future.
- 2) More advanced image fusion algorithms are needed to enhance and improve the adaptation to the fusion

needs of different materials and different defects in hypervelocity impacts of spacecraft.

- 3) The fused infrared detection results image should be taken further image processing and defect quantification algorithms to improve the accuracy and detectability of defects.

## REFERENCES

- [1] X. Huang, C. Yin, H. Ru, S. Zhao, Y. Deng, Y. Guo, and S. Liu, "Hypervelocity impact damage behavior of B4C/Al composite for MMOD shielding application," *Mater. Des.*, vol. 186, Jan. 2020, Art. no. 108323.
- [2] E. L. Christiansen, *Meteoroid/Debris Shielding*. Houston, TX, USA: National Aeronautics and Space Administration, Lyndon B. Johnson Space Center, 2003.
- [3] C. Yin, T. Xue, X. Huang, Y.-H. Cheng, S. Dadras, and S. Dadras, "Research on damages evaluation method with multi-objective feature extraction optimization scheme for M/OD impact risk assessment," *IEEE Access*, vol. 168, pp. 98530–98598, 2019.
- [4] J. Arnold, E. L. Christiansen, L. Eric, A. Davis, J. Hyde, D. Lear, J. C. Liou, F. Lyons, T. Prior, G. Studor, M. Ratliff, S. Ryan, G. Shannon, F. Corsaro, and B. Corsaro, "Handbook for designing MMOD protection," NASA Johnson Space Center, Houston, TX, USA, Tech. Rep. NASA/TM-2009-214785, 2009.
- [5] D. R. Green, "Principles and applications of emittance-independent infrared nondestructive testing," *Appl. Opt.*, vol. 7, no. 9, p. 1779, 1968.
- [6] Y. Cheng, C. Yin, Y. Chen, L. Bai, X. Huang, X. Zhou, and F. Yang, "ICA fusion approach based on fuzzy using in eddy current pulsed thermography," *Int. J. Appl. Electromagn. Mech.*, vol. 52, nos. 1–2, pp. 443–451, Dec. 2016.
- [7] B. Gao, W. L. Woo, Y. He, and G. Y. Tian, "Unsupervised sparse pattern diagnostic of defects with inductive thermography imaging system," *IEEE Trans. Ind. Informat.*, vol. 12, no. 1, pp. 371–383, Feb. 2016.
- [8] T. Liang, W. Ren, G. Y. Tian, M. Elradi, and Y. Gao, "Low energy impact damage detection in CFRP using eddy current pulsed thermography," *Compos. Struct.*, vol. 143, pp. 352–361, May 2016.
- [9] W. F. Da Silva, R. A. C. Melo, M. Grosso, G. R. Pereira, and D. B. Riffel, "Active thermography data-processing algorithm for nondestructive testing of materials," *IEEE Access*, vol. 8, pp. 175054–175062, 2020.
- [10] K. Kaur and R. Mulaveesala, "Active infrared imaging for estimation of sub-surface features in a steel material," *Procedia Comput. Sci.*, vol. 171, pp. 1204–1211, Jan. 2020.
- [11] J. Ahmad, A. Akula, R. Mulaveesala, and H. K. Sardana, "An independent component analysis based approach for frequency modulated thermal wave imaging for subsurface defect detection in steel sample," *Infr. Phys. Technol.*, vol. 98, pp. 45–54, May 2019.
- [12] X. Maldague, A. Ziadi, and M. Klein, "Double pulse infrared thermography," *NDT & E Int.*, vol. 37, no. 7, pp. 559–564, Oct. 2004.
- [13] L. Cheng, B. Gao, G. Y. Tian, W. L. Woo, and G. Berthiau, "Impact damage detection and identification using eddy current pulsed thermography through integration of PCA and ICA," *IEEE Sensors J.*, vol. 14, no. 5, pp. 1655–1663, May 2014.
- [14] R. Liu, Q. Shen, and H. Liu, "Emotion-specific facial activation maps based on infrared thermal image sequences," *IEEE Access*, vol. 16, pp. 735–742, 2019.
- [15] X. Xiao, B. Gao, W. L. Woo, G. Y. Tian, and X. T. Xiao, "Spatial-time-state fusion algorithm for defect detection through eddy current pulsed thermography," *Infr. Phys. Technol.*, vol. 90, pp. 133–145, May 2018.
- [16] R. Yang, Y. He, B. Gao, G. Y. Tian, and J. Peng, "Lateral heat conduction based eddy current thermography for detection of parallel cracks and rail tread oblique cracks," *Measurement*, vol. 66, pp. 54–61, Apr. 2015.
- [17] S. Zhang, C. Guo, L. Cheng, and H. Wang, "A far-field evaluation method for interfacial defects existed in composite insulators based on transient thermal wave," *IEEE Access*, vol. 7, pp. 1920–1926, 2019.
- [18] P. Zhu, C. Yin, Y. Cheng, X. Huang, J. Cao, C.-M. Vong, and P. K. Wong, "An improved feature extraction algorithm for automatic defect identification based on eddy current pulsed thermography," *Mech. Syst. Signal Process.*, vol. 113, pp. 5–21, Dec. 2018.
- [19] H. Zhang, X. Huang, C. Yin, Y.-H. Cheng, A. Shi, S. Dadras, and J. Luo, "Design of hypervelocity-impact damage evaluation technique based on Bayesian classifier of transient temperature attributes," *IEEE Access*, vol. 8, pp. 18703–18715, 2020.
- [20] J. Yang, W. Wang, G. Lin, Q. Li, Y. Sun, and Y. Sun, "Infrared thermal imaging-based crack detection using deep learning," *IEEE Access*, vol. 7, pp. 182060–182077, 2019.
- [21] X. Lu, Q. Yi, and G. Y. Tian, "A comparison of feature extraction techniques for delamination of CFRP using eddy current pulse-compression thermography," *IEEE Sensors J.*, vol. 20, no. 20, pp. 12415–12422, Oct. 2020.
- [22] K. Liu, Y. Li, J. Yang, Y. Liu, and Y. Yao, "Generative principal component thermography for enhanced defect detection and analysis," *IEEE Trans. Instrum. Meas.*, vol. 69, no. 10, pp. 8261–8269, Oct. 2020.
- [23] F. Wang, Y. Wang, J. Liu, and Y. Wang, "The feature recognition of CFRP subsurface defects using low-energy chirp-pulsed radar thermography," *IEEE Trans. Ind. Informat.*, vol. 16, no. 8, pp. 5160–5168, Aug. 2020.
- [24] C. Wu, Z. Liu, and H. Jiang, "Catenary image segmentation using the simplified PCNN with adaptive parameters," *Optik Int. J. Light Electron Opt.*, vol. 157, pp. 914–923, Mar. 2018.
- [25] S. F. Galán, "Comparative evaluation of region query strategies for DBSCAN clustering," *Inf. Sci.*, vol. 502, pp. 76–90, Oct. 2019.
- [26] Z. Li, Y. Li, W. Lu, and J. Huang, "Crowdsourcing logistics pricing optimization model based on DBSCAN clustering algorithm," *IEEE Access*, vol. 8, pp. 92615–92626, 2020.
- [27] Q. Zhang and H. Li, "MOEA/D: A multiobjective evolutionary algorithm based on decomposition," *IEEE Trans. Evol. Comput.*, vol. 11, no. 6, pp. 712–731, Dec. 2007.
- [28] K. Miettinen, *Nonlinear Multiobjective Optimization*. Springer, 2012.
- [29] W. Li, L. Jia, and J. Du, "Multi-modal sensor medical image fusion based on multiple salient features with guided image filter," *IEEE Access*, vol. 7, pp. 173019–173033, 2019.
- [30] R. Dian, S. Li, B. Sun, and A. Guo, "Recent advances and new guidelines on hyperspectral and multispectral image fusion," *Inf. Fusion*, vol. 69, pp. 40–51, May 2021.
- [31] J. Li, H. Huo, C. Sui, C. Jiang, and C. Li, "Poisson reconstruction-based fusion of infrared and visible images via saliency detection," *IEEE Access*, vol. 7, pp. 20676–20688, 2019.



**XUTONG TAN** received the B.Sc. degree in automation from the University of Electronic Science and Technology of China, Chengdu, China, in 2019, where he is currently pursuing the M.Sc. degree in control science and control engineering. His research interests include hypervelocity impact damage assessment, intelligent information processing, and machine learning.



**XUEGANG HUANG** received the B.S. degree majoring in materials science and engineering from Southwest Jiaotong University, and the M.S. and Ph.D. degrees from the Mechanical Engineering College, Shijiazhuang, China, in 2010 and 2014, respectively.

He has been working as an Associate Researcher with the Hypervelocity Aerodynamic Institute, Center of Aerodynamic Research and Develop of China, since 2014. His research interests include spacecraft measurement and control technology, space shielding engineering, hypervelocity impact engineering, and material dynamic behavior. He has published over 60 refereed journal articles in the above-mentioned fields. He currently serves as a Guest Editor for Special Issue "Artificial Intelligence for Space Environment and Spacecraft" in the journal of *Frontiers of Information Technology & Electronic Engineering*. His master's thesis was selected as the Excellent Master Dissertation of Hebei Province, in 2012, and his doctoral dissertation was selected as the National Excellent Doctoral Dissertation of China, in 2017.



**CHUN YIN** (Member, IEEE) received the Ph.D. degree from the University of Electronic Science and Technology of China, in 2014.

She was an Exchange Ph.D. Student with Utah State University, Logan, UT, USA, from 2011 to 2012. She was also an Exchange Ph.D. Student with the University of California Merced, Merced, CA, USA, from 2012 to 2013. She was an Associate Professor with the University of Electronic Science and Technology of China, from 2014 to 2019. She has been a Professor with the School of Automation Engineering, University of Electronic Science and Technology of China, since 2019. Seven of her articles have been listed as *Hot Paper* by Essential Science Indicators (ESI). One of her articles have been selected as the Top five list of Highly Cited Research in the journal of *Mechatronics*, and one of her articles have been selected as the ScienceDirect Top 25 list of Most Download Articles. Her research interests include multi-objective evolutionary optimization, infrared thermography testing, and hypervelocity impact engineering. She received the Overall Best Paper Award in 2015 IEEE International Instrumentation and Measurement Technology Conference. One of her technological achievements obtained the first prize for Scientific and Technological Progress awards of Sichuan Province. She currently serves as a Guest Editor for Special Issue “Artificial Intelligence for Space Environment and Spacecraft” in the journal of *Frontiers of Information Technology & Electronic Engineering*.



**SARA DADRAS** (Senior Member, IEEE) received the B.Sc. degree in electrical engineering from Shiraz University, in 2006, and the M.Sc. and Ph.D. degrees in electrical engineering from Tarbiat Modares University, in 2008 and 2012, respectively. She joined the Electrical and Computer Engineering Department, Utah State University, in 2012, as a Research Fellow. Her current research interests include hybrid electric vehicles, autonomous vehicles, renewable energy systems,

image processing, and optimal controls. She is also the Organizer of SAE Electronics Technical Committee. She currently serves as an Associate Editor for IEEE TRANSACTIONS ON AUTOMATION SCIENCE AND ENGINEERING, IEEE ACCESS, *Asian Journal of Control*, and *Complexity*. She also serves as a Guest Editor for Special Issue “Artificial Intelligence for Space Environment and Spacecraft” in the journal of *Frontiers of Information Technology & Electronic Engineering*.



**YU-HUA CHENG** (Senior Member, IEEE) received the M.S. degree from Xihua University, in 2004, and the Ph.D. degree majoring in measurement technology and industrial automation from Sichuan University, Chengdu, China, in 2007. He is currently working as a Professor with the University of Electronic Science and Technology of China. His research interests include industrial automation and instrumentation, damage detection technique, and fault diagnosis.



**ANHUA SHI** received the B.Sc. degree in fluid mechanics from the Nanjing University of Aeronautics and Astronautics, Nanjing, China, in 2002. He is currently working as a Professor with the Hypervelocity Aerodynamic Institute, Center of Aerodynamic Research and Develop of China. His research interests include infrared thermal imaging, radiation detection technology, and digital image recognition.

...